JOURNAL OF COMPUTATIONAL PHYSICS 98, 33–53 (1992)

An Interactive Approach for Calculating Ship Boundary Layers and Wakes for Nonzero Froude Number

Y. TAHARA, F. STERN

Iowa Institute of Hydraulic Research, The University of Iowa, Iowa City, Iowa 52242

AND

B. ROSEN

South Bay Simulations Inc., 44 Sumpwams Ave., Babylon, New York 11702

Received August 1, 1990; revised December 11, 1990

An interactive approach is set forth for calculating ship boundary layers and wakes for nonzero Froude number. The Reynolds-averaged Navier–Stokes equations are solved using a small domain with edge conditions matched with those from a source-doublet Dawson method solved using the displacement body. An overview is given of both the viscous- and inviscid-flow methods, including their treatments of the free-surface boundary conditions and interaction procedures. Results are presented for the Wigley hull, including comparisons for zero and nonzero Froude number and with available experimental data and the inviscid-flow results, which validate the overall approach and enable an evaluation of the wave-boundary layer and wake interaction.

INTRODUCTION

The interaction between the wavemaking of a ship and its boundary layer and wake is a classic and important problem in ship hydrodynamics. Initially, the interest was primarily with viscous effects on wave resistance and propulsive performance due to the lack of Reynolds number (Re) similarity in model tests. More recently, also of interest are the wave-boundary layer and wake interaction effects on the details of ship wakes and wave patterns due to the advent of satellite remote sensing. The present study is central to the aforementioned problems; i.e., it concerns the development of an interactive approach for calculating ship boundary layers and wakes for nonzero Froude number (Fr). Thus, both the effects of wavemaking on the boundary layer and wake and, vice versa, the effects of the boundary layer and wake on wavemaking are included in the theory, although the focus here is somewhat more on the former.

Historically, inviscid-flow methods have been used to calculate wavemaking and viscous-flow methods the boundary layer and wake, in both cases, without accounting for the interaction. Recent work on wavemaking has focused on the solution of the so-called Neumann–Kelvin problem using both Rankine- and Havelock-source approaches. Method implementing these approaches were recently competitively evaluated and ranked by comparing their results with towing-tank experimental data [1]. In general, the methods underpredicted the amplitude of the divergent bow waves, were lacking in high wave-number detail in the vicinity of the bow-wave cusp line, and overpredicted the amplitudes of the waves close to the stern. These difficulties were primarily attributed to nonlinear and viscous effects. The methods using the Havelock-source approach generally outperformed those using the Rankine-source approach, except with regard to the near-field results (i.e., within one beam length of the model) for which one of the latter methods [2] was found to be far superior.

Considerable effort has been put forth in the development of viscous-flow methods for ship boundary layers and wakes. Initially, three-dimensional integral and differential boundary-layer equation methods were developed; however, these were found to be inapplicable near the stern and in the wake. More recently, efforts have been directed towards the development of Navier–Stokes (NS) and Reynolds-averaged Navier–Stokes (RANS) equation methods; hereafter both of these will simply be referred to as RANS equation methods. At present, the status of these methods is such that practical ship geometries can be considered, including complexities such as appendages and propellers. Comparisons with experimental data indicate that many features of the flow are adequately simulated; however, turbulence modeling and grid generation appear to be pacesetting issues with regard to future developments (see, e.g., the review by Patel [3] and the *Proceedings of the 5th International Conference on Numerical Ship Hydrodynamics* [4]).

0021-9991/92 $3.00

Relatively little work has been done on the interaction between wavemaking and boundary layer and wake. Most studies have focused separately on either the effects of viscosity on wavemaking or the effects of wavemaking (i.e., waves) on the boundary layer and wake. Professor Landweber and his students have both demonstrated experimentally the dependence of wave resistance on viscosity and shown computationally that by including the effects of viscosity in inviscid-flow calculations of wave resistance better agreement with experimental data is obtained (most recently, [5]). Such effects have been confirmed by others, including other more detailed aspects of the flow field such as surface-pressure distributions and wave profiles and patterns [6].

Most studies concerning the effects of waves on boundary layer and wake have been of an approximate nature, utilizing integral methods and assuming small crossflow conditions (see Stern [7] for a more complete review, including references). In [7, 8], experiment and theory are combined to study the fundamental aspects of the problem utilizing a unique, simple model and computational geometry, which enabled the isolation and identification of certain important features of the wave-induced effects. In particular, the variations of the wave-induced piezometric-pressure gradients are shown to cause acceleration and deceleration phases of the streamwise velocity component and alternating direction of the crossflow, which results in large oscillations of the displacement thickness and wall-shear stress as compared to the no-wave condition. For the relatively simple geometry studied, first-order boundary-layer calculations with a symmetry-condition approximation for the free-surface boundary conditions were shown to be satisfactory; however, extensions of the computational approach for practical geometries were not successful [9].

Miyata *et al.* [10] and Hino [11] have pursued a comprehensive approach to the present problem in which the NS equations (sub-grid scale and Reynolds averaged, respectively) are solved using a large domain with approximate free-surface boundary conditions. In both cases, the basic algorithms closely follow those of MAC [12] and SUMMAC [13]. However, [10] uses a time-dependent free-surface conforming grid, whereas [11] uses a fixed grid which does not conform to the free surface. The results from both approaches are promising, but, thus far, have had difficulties in accurately resolving the boundary-layer and wake regions and, in the case of [10], have been limited to low Re.

The present interactive approach is also comprehensive. Two of the leading inviscid- [2] and viscous-flow [14] methods are modified and extended for interactive calculations for ship boundary layers and wakes for nonzero Fr. The interaction procedures are based on extensions of those developed by one of the authors for zero Fr [15]. The work of [7, 8, 15] is precursory to the present study. Also, it should be mentioned that the present study is part of a large project concerning free-surface effects on boundary layers and wakes. Some of the related studies under this project will be referenced later.

In the following, an overview is given of both the viscous- and inviscid-flow methods, with particular emphasis on their treatments of the free-surface boundary conditions and the interaction procedures. Results are presented for the Wigley hull, including comparisons for zero and nonzero Fr and with available experimental data and inviscid-flow results, which validate the overall approach and enable an evaluation of the wave-boundary layer and wake interaction. In the presentation of the computational methods and results and discussions to follow, variables are either defined in the text or in the Appendix and are nondimensionalized using the ship length L, freestream velocity U_o, and fluid density ρ.

COMPUTATIONAL METHODS

Consider the flow past a ship-like body, moving steadily at velocity U_o, and intersecting the free surface of an incompressible viscous fluid. As depicted in Fig. 1, the flow field can be divided into four regions in each of which different or no approximations can be made to the governing RANS equations: region 1 is the inviscid flow; region 2 is the bow flow; region 3 is the thin boundary layer; and region 4 is the thick boundary layer and wake. The resulting equations for regions 1 and 3 and their interaction (or lack of one) are well known. Relatively little is known about region 2. Recent experiments concerning scale effects on near-field wave patterns have indicated a Re dependency for the bow wave both in amplitude and divergence angle [16]; however, this aspect of the problem is deferred for later study. Herein, we are primarily concerned with the flow in region 4 and its interaction with that in region 1. As discussed earlier, the description of the flow in region 4 requires the solution of the complete RANS equations (or, in the absence of flow reversal, the so-called partially parabolic RANS equations, however, this simplification will not be considered here).

There are two possible approaches to the solution of the RANS equations: a global approach, in which one set of governing equations appropriate for both the inviscid- and viscous-flow regions are solved using a large solution domain so as to capture the viscous–inviscid interaction; and an interactive approach, in which different sets of governing equations are used for each region and the complete solution obtained through the use of an interaction law, i.e., patching or matching conditions. Both approaches are depicted in Fig. 1. The former approach is somewhat more rigorous because it does not rely on the patching conditions that usually involve approximations. Nonetheless, for a variety of reasons, both types of approaches are of

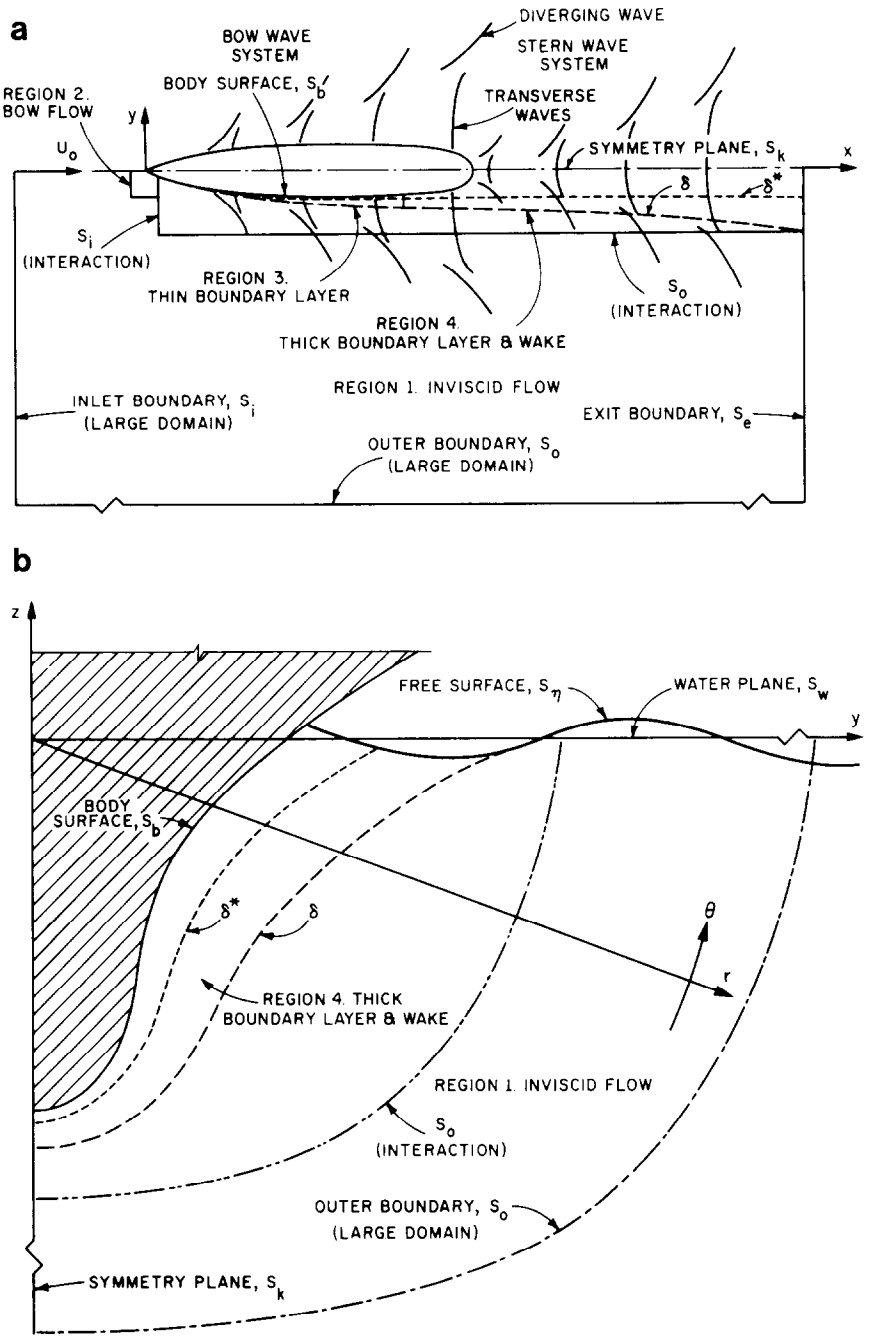

FIG. 1. Definition sketch of flow-field regions and solution domains: (a) (x, y) plane; (b) (y, z) plane.

interest. In [15], both approaches were evaluated for zero Fr by comparing interactive and large-domain solutions for axisymmetric and simple three-dimensional bodies using the same numerical techniques and algorithms and turbulence model. It is shown that both approaches yield satisfactory results, although the interaction solutions appear to be computationally more efficient. As mentioned earlier, the present study utilizes the interactive approach. This takes advantage of the latest developments in both the inviscid- and viscous-flow technologies; however, a large-domain solution for the present problem is also of interest and a comparative evaluation as was done previously for zero Fr is planned for study under the present project for nonzero Fr.

Viscous–Inviscid Interaction

Referring to Fig. 1, there are two primary differences between the interactive and large-domain approaches with regard to the solution of the RANS equations: (1) the size

of the solution domain, i.e., the placement of the outer boundary S_o; and (2) the boundary (i.e., edge) conditions specified thereon. For the large-domain solution, uniform-flow and wave-radiation conditions are appropriate, whereas the interaction solution requires the specification of the match boundary (i.e., S_o), as well as an interaction law, and also a method for calculating the inviscid flow.

In the present study, solutions were obtained with the match boundary at about 2δ, where δ is the boundary layer and wake thickness. The interaction law is based on the concept of displacement thickness δ^*. A three-dimensional δ^* for a thick boundary layer and wake can be defined unambiguously by the two requirements that it be a stream surface of the inviscid flow continued from outside the boundary layer and wake and that the inviscid-flow discharge between this surface and any stream surface exterior to the boundary layer and wake be equal to the actual discharge between the body and wake centerplane and the latter stream surface. A method for implementing this definition for practical geometries is presently under development [17]; however, in lieu of this, an approximate definition is used in which two-dimensional definitions for δ^*, i.e.,

$$\delta^* = \int_0^{\delta} \left(1 - \frac{U}{U_p}\right) dr \tag{1}$$

for the keelplane and waterplane at each station are connected by a second-order polynomial.

In summary, the inviscid-flow solution is obtained for the displacement body δ^*. This solution then provides the boundary conditions for the viscous-flow solution, i.e.,

$$\begin{aligned} U(S_o) &= U_p(S_o) = U_e, \\ W(S_o) &= W_p(S_o) = W_e, \\ p(S_o) &= p_p(S_o) = p_e. \end{aligned} \tag{2}$$

Because δ^* and $\mathbf{V}_p(S_o)$ are not known a priori, an initial guess must be provided and the complete solution obtained by iteratively updating the viscous- and inviscid-flow solutions until the patching conditions (1) and (2) are satisfied.

Viscous Flow

The viscous flow is calculated using the large-domain method of Patel *et al.* [14] modified and extended for interactive calculations and to include free-surface boundary conditions. The details of the basic method are provided by [14]. Herein, an overview is given as an aid in understanding the present modifications and extensions.

Equations and Coordinate System

The RANS equations are written in the physical domain using cylindrical coordinates (x, r, θ) as

$$\frac{\partial U}{\partial x} + \frac{1}{r}\frac{\partial}{\partial r}(rV) + \frac{1}{r}\frac{\partial W}{\partial \theta} = 0, \tag{3}$$

$$\frac{DU}{Dt} = -\frac{\partial}{\partial x}(\hat{p} + \overline{uu}) - \frac{\partial}{\partial r}(\overline{uv}) - \frac{1}{r}\frac{\partial}{\partial \theta}(\overline{uw}) - \frac{\overline{uv}}{r} + \frac{1}{\mathrm{Re}}\nabla^2 U, \tag{4}$$

$$\frac{DV}{Dt} - \frac{W^2}{r} = -\frac{\partial}{\partial x}(\overline{uv}) - \frac{\partial}{\partial r}(\hat{p} + \overline{vv}) - \frac{1}{r}\frac{\partial}{\partial \theta}(\overline{vw}) - \frac{1}{r}(\overline{vv} - \overline{ww}) + \frac{1}{\mathrm{Re}}\left(\nabla^2 V - \frac{2}{r^2}\frac{\partial W}{\partial \theta} - \frac{V}{r^2}\right), \tag{5}$$

$$\frac{DW}{Dt} + \frac{VW}{r} = -\frac{\partial}{\partial x}(\overline{uw}) - \frac{\partial}{\partial r}(\overline{vw}) - \frac{1}{r}\frac{\partial}{\partial \theta}(\hat{p} + \overline{ww}) - \frac{2}{r}(\overline{vw}) + \frac{1}{\mathrm{Re}}\left(\nabla^2 W + \frac{2}{r^2}\frac{\partial V}{\partial \theta} - \frac{W}{r^2}\right), \tag{6}$$

with

$$\frac{D}{Dt} = \frac{\partial}{\partial t} + U\frac{\partial}{\partial x} + V\frac{\partial}{\partial r} + \frac{W}{r}\frac{\partial}{\partial \theta},$$

and

$$\nabla^2 = \frac{\partial^2}{\partial x^2} + \frac{\partial^2}{\partial r^2} + \frac{1}{r}\frac{\partial}{\partial r} + \frac{1}{r^2}\frac{\partial^2}{\partial \theta^2}.$$

Closure of the RANS equations is attained through the use of the standard $k-\varepsilon$ turbulence model without modifications for free-surface effects. The limited experimental data available for surface-piercing bodies [18] indicate that, near a free surface, the normal component of turbulence is damped and the longitudinal and transverse components are increased. This effect has also been observed in open-channel flow [19] and in recent measurements for free-surface effects on the wake of a submerged flat plate [20] and a plane jet [21]. Such a turbulence structure cannot, in fact, be simulated with an isotropic eddy viscosity turbulence model like the present one; however, this aspect of the problem is also deferred for later study.

In the standard $k-\varepsilon$ turbulence model, each Reynolds

stress is related to the corresponding mean rate of strain by the isotropic eddy viscosity ν_t as

$$
\begin{aligned}
-\overline{uv} &= \nu_t\left(\frac{\partial U}{\partial r}+\frac{\partial V}{\partial x}\right),\\
-\overline{uw} &= \nu_t\left(\frac{1}{r}\frac{\partial U}{\partial \theta}+\frac{\partial W}{\partial x}\right),\\
-\overline{vw} &= \nu_t\left(\frac{1}{r}\frac{\partial V}{\partial \theta}+\frac{\partial W}{\partial r}-\frac{W}{r}\right),\\
-\overline{uu} &= \nu_t\left(2\frac{\partial U}{\partial x}\right)-\frac{2}{3}k,\\
-\overline{vv} &= \nu_t\left(2\frac{\partial V}{\partial r}\right)-\frac{2}{3}k,\\
-\overline{ww} &= \nu_t\left(\frac{2}{r}\frac{\partial W}{\partial \theta}+2\frac{V}{r}\right)-\frac{2}{3}k;
\end{aligned}
\tag{7}
$$

ν_t is defined in terms of the turbulent kinetic energy k and its rate of dissipation ε by

$$
\nu_t = C_\mu \frac{k^2}{\varepsilon}, \tag{8}
$$

where C_μ is a model constant and k and ε are governed by the modeled transport equations

$$
\begin{aligned}
\frac{Dk}{Dt} &= \frac{\partial}{\partial x}\left(\frac{1}{R_k}\frac{\partial k}{\partial x}\right)+\frac{1}{r}\frac{\partial}{\partial r}\left(\frac{1}{R_k}r\frac{\partial k}{\partial r}\right)\\
&\quad+\frac{1}{r^2}\frac{\partial}{\partial \theta}\left(\frac{1}{R_k}\frac{\partial k}{\partial \theta}\right)+G-\varepsilon,
\end{aligned}
\tag{9}
$$

$$
\begin{aligned}
\frac{D\varepsilon}{Dt} &= \frac{\partial}{\partial x}\left(\frac{1}{R_\varepsilon}\frac{\partial \varepsilon}{\partial x}\right)+\frac{1}{r}\frac{\partial}{\partial r}\left(\frac{1}{R_\varepsilon}r\frac{\partial \varepsilon}{\partial r}\right)\\
&\quad+\frac{1}{r^2}\frac{\partial}{\partial \theta}\left(\frac{1}{R_\varepsilon}\frac{\partial \varepsilon}{\partial \theta}\right)+C_{\varepsilon 1}\frac{\varepsilon}{k}G-C_{\varepsilon 2}\frac{\varepsilon^2}{k}.
\end{aligned}
\tag{10}
$$

G is the turbulence generation term,

$$
\begin{aligned}
G = \nu_t\Bigg\{&2\left[\left(\frac{\partial U}{\partial x}\right)^2+\left(\frac{\partial V}{\partial r}\right)^2+\left(\frac{1}{r}\frac{\partial W}{\partial \theta}+\frac{V}{r}\right)^2\right]\\
&+\left(\frac{\partial U}{\partial r}+\frac{\partial V}{\partial x}\right)^2+\left(\frac{1}{r}\frac{\partial U}{\partial \theta}+\frac{\partial W}{\partial x}\right)^2\\
&+\left(\frac{1}{r}\frac{\partial V}{\partial \theta}+\frac{\partial W}{\partial r}-\frac{W}{r}\right)^2\Bigg\}.
\end{aligned}
\tag{11}
$$

The effective Re R_ϕ is defined as

$$
\frac{1}{R_\phi} = \frac{1}{\mathrm{Re}}+\frac{\nu_t}{\sigma_\phi} \tag{12}
$$

in which $\phi = k$ for the k-equation (9) and $\phi = \varepsilon$ for the ε-equation (10). The model constants are: $C_\mu = 0.09$, $C_{\varepsilon 1} = 1.44$, $C_{\varepsilon 2} = 1.92$, $\sigma_U = \sigma_V = \sigma_W = \sigma_k = 1$, $\sigma_\varepsilon = 1.3$.

The governing equations (3) through (12) are transformed into nonorthogonal curvilinear coordinates such that the computational domain forms a simple rectangular parallelepiped with equal grid spacing. The transformation is a partial one since it involves the coordinates only and not the velocity components (U, V, W). The transformation is accomplished through use of the expression for the divergence and "chain-rule" definitions of the gradient and Laplacian operators which relate the orthogonal curvilinear coordinates $x^i = (x, r, \theta)$ to the nonorthogonal curvilinear coordinates $\xi^i = (\xi, \eta, \zeta)$. In this manner, the governing equations (3) through (12) can be rewritten in the form of the continuity and convective-transport equations

$$
\begin{aligned}
&\frac{\partial}{\partial \xi}(b_1^1 U+b_2^1 V+b_3^1 W)+\frac{\partial}{\partial \eta}(b_1^2 U+b_2^2 V+b_3^2 W)\\
&\qquad+\frac{\partial}{\partial \zeta}(b_1^3 U+b_2^3 V+b_3^3 W)=0,
\end{aligned}
\tag{13}
$$

$$
\begin{aligned}
&g^{11}\frac{\partial^2 \phi}{\partial \xi^2}+g^{22}\frac{\partial^2 \phi}{\partial \eta^2}+g^{33}\frac{\partial^2 \phi}{\partial \zeta^2}\\
&\qquad=2A_\phi\frac{\partial \phi}{\partial \zeta}+2B_\phi\frac{\partial \phi}{\partial \eta}+2C_\phi\frac{\partial \phi}{\partial \xi}+R_\phi\frac{\partial \phi}{\partial t}+S_\phi.
\end{aligned}
\tag{14}
$$

Discretization and Velocity-Pressure Coupling

The convective-transport equations (14) are reduced to algebraic form through the use of a revised and simplified version of the finite-analytic method. In this method, Eqs. (14) are linearized in each local rectangular numerical element, $\Delta\xi = \Delta\eta = \Delta\zeta = 1$, by evaluating the coefficients and source functions at the interior node P and transformed again into a normalized form by a simple coordinate stretching. An analytic solution is derived by decomposing the normalized equation into one- and two-dimensional partial differential equations. The solution to the former is readily obtained. The solution to the latter is obtained by the method of separation of variables with specified boundary functions. As a result, a 12-point finite-analytic formula for unsteady, three-dimensional, elliptic equations is obtained in the form

$$
\begin{aligned}
\phi_P &= \frac{1}{1+C_P[C_U+C_D+(R/\tau)]}\\
&\quad\times\left\{\sum_1^8 C_{nb}\phi_{nb}+C_P\left(C_U\phi_U+C_D\phi_D+\frac{R}{\tau}\phi_P^{n-1}-S\right)\right\}.
\end{aligned}
\tag{15}
$$

It is seen that ϕ_P depends on all eight neighboring nodal values in the crossplane as well as the values at the upstream

and downstream nodes ϕ_U and ϕ_D, and the values at the previous time step ϕ_P^{n-1}. For large values of the cell Re, Eq. (15) reduces to the partially parabolic formulation which was used previously in other applications. Since Eq. (15) are implicit, both in space and time, at the current crossplane of calculation, their assembly for all elements results in a set of simultaneous algebraic equations. If the pressure field is known, these equations can be solved by the method of lines. However, since the pressure field is unknown, it must be determined such that the continuity equation is also satisfied.

The coupling of the velocity and pressure fields is accomplished through the use of a two-step iterative procedure involving the continuity equation based on the SIMPLER algorithm. In the first step, the solution to the momentum equations for a guessed pressure field is corrected at each crossplane such that continuity is satisfied. However, in general, the corrected velocities are no longer a consistent solution to the momentum equations for the guessed $\hat{p}$. Thus, the pressure field must also be corrected. In the second step, the pressure field is updated again through the use of the continuity equation. This is done after a complete solution to the velocity field has been obtained for all crossplanes. Repeated global iterations are thus required in order to obtain a converged solution. The procedure is facilitated through the use of a staggered grid. Both the pressure-correction and pressure equations are derived in a similar manner by substituting Eq. (15) for (U, V, W) into the discretized form of the continuity equation (13) and representing the pressure-gradient terms by finite differences.

Solution Domain and Boundary Conditions

The solution domain is shown in Fig. 1. In terms of the notation of Fig. 1, the boundary conditions on each of the boundaries are as follows: *On the inlet plane* S_i, the initial conditions for ϕ are specified from simple flat-plate and the inviscid-flow solutions. *On the body surface* S_b, a two-point wall-function approach is used. *On the symmetry plane* S_k, the conditions imposed are $\partial(U, V, \hat{p}, k, \varepsilon)/\partial\theta = W = 0$. *On the exit plane* S_e, axial diffusion is negligible so that the exit conditions used are $\partial^2\phi/\partial x^2 = 0$, and a zero-gradient condition is used for $\hat{p}$. *On the outer boundary* S_o, the edge conditions are specified according to (2), i.e., $(U, W, \hat{p}) = (U_e, W_e, \hat{p}_e)$ and $\partial(k, \varepsilon)/\partial r = 0$, where $(U_e, W_e, \hat{p}_e)$ are obtained from the inviscid-flow solution evaluated at the match boundary S_o.

On the free-surface S_η (or simply η), there are two boundary conditions, i.e.,

$$\mathbf{V} \cdot \mathbf{n} = 0 \tag{16}$$

and

$$\tau_{ij} n_j = \tau_{ij}^* n_j, \tag{17}$$

where $\mathbf{n}$ is the unit normal vector to the free surface and τ_{ij} and τ_{ij}^* are the fluid- and external-stress tensors, respectively, the latter, for convenience, including surface tension. The kinematic boundary condition expresses the requirement that η is a stream surface and the dynamic boundary condition that the normal and tangential stresses are continuous across it. Note that η itself is unknown and must be determined as part of the solution. In addition, boundary conditions are required for the turbulence parameters, k and ε; however, at present, these are not well established.

In the present study, the following approximations were made in employing (16) and (17): (a) the external stress and surface tension were neglected; (b) the normal viscous stress and both the normal and tangential Reynolds stresses were neglected; (c) the curvature of the free surface was assumed small and the tangential gradients of the normal velocity components were neglected in the tangential stresses; and (d) the wave elevation was assumed small such that both (16) and (17) were represented by first-order Taylor series expansions about the mean wave-elevation surface (i.e., the waterplane S_w). Subject to these approximations, (16) and (17) reduce to

$$(U_x \eta_x + V_y \eta_y - W_z)|_{S_w} = 0, \tag{18}$$

$$\hat{p}(S_w) = \eta/\mathrm{Fr}^2 - \eta \left.\frac{\partial \hat{p}}{\partial z}\right|_{S_w}, \tag{19}$$

$$\left.\frac{\partial(\mathbf{V}, k, \varepsilon)}{\partial\theta}\right|_{S_w} = 0, \tag{20}$$

where Cartesian coordinates (x, y, z) have been used in (18) and (19). Conditions (18) through (20) were implemented numerically as follows: The kinematic condition (18) was used to solve for the unknown free-surface elevation η by expressing the derivatives in finite-difference form and η in terms of its difference from an assumed (or previous) value. A backward difference was used for the x-derivative, a central difference for the y-derivative, and the inviscid-flow η_p was used as an initial guess. The dynamic conditions, (19) and (20), were used in conjunction with the solution for η in solving the pressure and momentum and turbulence model equations, respectively. Backward differences were used for the z- and θ-derivatives.

Inviscid Flow

The inviscid flow is calculated using the method of Rosen [2], i.e., the SPLASH computer code. The method is an extended version of the basic panel method of Maskew [22, 23] originally developed for the prediction of subsonic aerodynamic flows about arbitrary configurations, modified to include the presence of a free surface and gravity waves both for submerged and surface-piercing bodies. As is the

case with the basic method, lifting surfaces and their associated wake treatments as well as wall boundaries are included; however, the present overview and calculations are for nonlifting unbounded flow (see [24] for SPLASH results for lifting flow). The details of the basic method are provided by [22, 23]. Herein, an overview is given as an aid in understanding the extensions for the inclusion of the free surface and gravity waves and the present interaction calculations.

The flow is assumed irrotational such that the governing differential equation is the Laplace equation

$$\nabla^2\phi = 0, \tag{21}$$

where ϕ is the external perturbation velocity potential; i.e.,

$$\mathbf{V}_p = U_o x + \nabla\phi. \tag{22}$$

A solution for ϕ may be obtained by defining also an internal perturbation potential ϕ_I and applying Green's theorem to both the inner and outer regions and combining the resulting expressions to obtain

$$\phi = -\int_{S_b} \left\{ \mu \frac{\partial}{\partial n_Q}\left(\frac{1}{R_{PQ}}\right) + \frac{\sigma}{R_{PQ}} \right\} dS, \tag{23}$$

where R_{PQ} is the distance from the surface point Q to the field point P and $\mu = \phi_I - \phi$ and $\sigma = \partial(\phi - \phi_I)/\partial n_Q$ are the dipole and source strengths, respectively. In [22], the nature of solutions to (23) is investigated for two different specifications for ϕ_I, i.e., $\phi_I = 0$ and $U_o x$. In both cases, (23) is solved for the surface potential (i.e., $\phi(S_b)$) by representing the body by flat quadrilateral panels over which μ and σ are assumed constant and utilizing the farfield $\phi \to 0$ and body $\partial\phi/\partial n = -U_o n_x$ boundary conditions. The zero internal perturbation potential formulation ($\phi_I = 0$) is shown to produce "results of comparable accuracy to those from higher-order methods for the same density of control points." In this case, the velocity normal to the external surface V_n is

$$V_n = U_o n_x + \partial\phi/\partial n = U_o n_x + \sigma \tag{24}$$

and, the velocity tangent to the external surface V_t is

$$V_t = U_o t_x + \partial\phi/\partial t = U_o t_x - \partial\mu/\partial t, \tag{25}$$

where t_x is the x-component of a tangent vector and t is arclength in a tangential direction. For solid surfaces, V_n is usually zero, but it may be a specified nonzero value to simulate body motion, boundary-layer growth, inflow and outflow, control-surface deflection, etc. Hence, in the basic method, (24) is used to evaluate the source strengths directly. The corresponding doublet strengths are then given by solution of the discretized form of (23). Values of V_t are subsequently computed using (25) with a central difference for the t-derivative. It should be recognized that the so-called zero internal perturbation formulation is, in fact, equivalent to methods based on Green's third formula applied directly to the external perturbation potential (e.g., [25]).

In the SPLASH code, the internal zero-peturbation boundary condition is satisfied not only inside the submerged portion of the configuration, but also on the "other side" of a finite portion of the free surface. Both are represented by source-doublet singularity panels and flow leakage from one side of the free-surface to the other, at the free-surface outer boundary, is assumed to be negligible. This assumption is valid if the outer boundary of the free surface is sufficiently far from the configuration, and if the wave disturbances are eliminated before reaching the free-surface outer boundary. In this case, the discretized form of (23) is

$$\phi_i = \sum_{S_b + S_w} A_{ij}\mu_j + \sum_{S_b + S_w} B_{ij}\sigma_j = 0. \tag{26}$$

The free-surface shape is determined by representing the undisturbed free surface by panels, whereupon free-surface boundary conditions linearized with respect to zero Fr are imposed [26]. The zero Fr velocities, U_o, V_o, and W_o, are obtained by first considering all free-surface panels as solid and fixed (in contrast to a traditional approach which employs the double panel or image model). The nonzero Fr velocities are then expressed as small increments to those for zero Fr. The velocities tangent and normal to a free-surface panel are, respectively,

$$U_x \approx U_o + \Delta U, \qquad V_y \approx V_o + \Delta V, \tag{27}$$

and

$$V_n = W_z \approx W_o + \Delta W \approx \Delta W, \tag{28}$$

since $W_o = 0$ for a free-surface panel. Through Bernoulli's equation, the pressure on free-surface panels is a function of local velocity and is approximated by retaining only first-order incremental velocity terms

$$\begin{aligned} \hat{p} &= \tfrac{1}{2}\{1 - (U_x^2 + V_y^2 + W_z^2)\} \\ &\approx \tfrac{1}{2}\{1 - (U_o^2 + V_o^2)\} - \{U_o \Delta U + V_o \Delta V\} \\ &\approx \tfrac{1}{2}\{1 - (U_o^2 + V_o^2)\} \\ &\quad - \{U_o(U_x - U_o) + V_o(V_y - V_o)\}. \end{aligned} \tag{29}$$

Free-surface boundary conditions are linearized in a similar manner, retaining only first-order incremental

velocity and surface-elevation terms. The kinematic free-surface boundary condition (18) is approximated by

$$W_z = V_n \approx U_o \eta_x + V_o \eta_y \approx (U_o^2 + V_o^2)^{1/2} \eta_{so}, \quad (30)$$

where the subscript s_o denotes differentiation along a zero Fr streamline. The dynamic free-surface boundary condition (19), after differentiation along s_o, and substituting for η_{so} from (30), becomes

$$\frac{\partial \hat{p}}{\partial s_o} \approx \frac{1}{\mathrm{Fr}^2} \frac{V_n}{(U_o^2 + V_o^2)^{1/2}}. \quad (31)$$

A five-point backward difference is used in the ξ and η directions and the free-surface grid metrics are used to compute the pressure gradient

$$\frac{\partial \hat{p}}{\partial s_o} = \frac{U_o \dfrac{\partial \hat{p}}{\partial x} + V_o \dfrac{\partial \hat{p}}{\partial y}}{(U_o^2 + V_o^2)^{1/2}} = \frac{U_o \left(\dfrac{\partial \hat{p}}{\partial \xi} \dfrac{\partial \xi}{\partial x} + \dfrac{\partial \hat{p}}{\partial \eta} \dfrac{\partial \eta}{\partial x} \right) + V_o \left(\dfrac{\partial \hat{p}}{\partial \xi} \dfrac{\partial \xi}{\partial y} + \dfrac{\partial \hat{p}}{\partial \eta} \dfrac{\partial \eta}{\partial y} \right)}{(U_o^2 + V_o^2)^{1/2}}. \quad (32)$$

The pressure-gradient algorithm is structured to permit the use of any blocked free-surface grid arrangement. Also, using less than a five-point backward difference tends to dampen wave amplitudes. This wave-damping mechanism is employed on panels near the outer boundary of the finite free-surface model, so that wave disturbances are eliminated before reaching the free-surface outer boundary.

At this point, a sufficient number of linear dependencies have been established to permit the elimination of the unknown free-surface source strengths in (26), i.e., (24) relates source strength to panel normal velocity, (31) relates free-surface panel normal velocity to streamwise pressure gradient, (32) with backward differences relates streamwise pressure gradient to free-surface pressures, (29) relates free-surface pressure to free-surface panel tangential velocities, (25) relates panel tangential velocities to the local surface gradient of doublet strength, and central differences relate the local surface gradient of doublet strength to doublet strenghts. Hence, free-surface source strengths can be expressed as a linear combination of free-surface doublet strengths, i.e.,

$$\sigma_j = a_j + \sum_{S_w} b_{jk} \mu_k. \quad (33)$$

Substituting for σ_j from (33) into (26) yields

$$\phi_i = \sum_{S_b + S_w} A_{ij} \mu_j + \sum_{S_b} B_{ij} \sigma_j + \sum_{S_w} B_{ij} \left(a_j + \sum_{S_w} b_{jk} \mu_k \right). \quad (34)$$

With free-surface source strengths eliminated and source strengths on the solid body evaluated directly, solution of (34) yields the corresponding doublet strengths. The free-surface source strengths are then given by (33), and (24) and (25) are used to compute the resulting velocities on both body and free-surface panels. Pressures on free-surface panels are given by (29). A similar linearized formula is used for pressures acting on body panels, and configuration forces and moments are obtained by panel pressure integration.

For interactive calculations, the SPLASH code calculates the inviscid free-surface flow about the equivalent displacement body resulting from the previous viscous calculation. For this purpose, the equivalent displacement body is treated as a solid fixed surface. The inviscid flow velocities required for the next viscous flow calculation, at off-body points on the viscous grid outer boundary S_o, are obtained using the computed source-doublet solution and velocity influence coefficients. A sub-panel velocity influence-coefficient algorithm was developed which utilizes a bilinear variation of source and doublet strength across each panel. The continuous variation of source and doublet strength on each panel, and across panel edges, enhances the accuracy of off-body velocity calculations at points close to any body and/or free-surface panels.

WIGLEY HULL GEOMETRY AND EXPERIMENTAL INFORMATION

The Wigley parabolic hull was selected for the initial calculations since the geometry is relatively simple and it has been used in many previous computational and experimental studies. In particular, it is one of the two hulls, the other being the Series 60 $C_B = 0.6$ ship model, selected by the Cooperative Experimental Program (CEP) of the Resistance and Flow Committee of the International Towing Tank Conference [27] for which extensive global (total, wave pattern, and viscous resistance, mean sinkage and trim, and wave profiles on the hull) and local (hull pressure and wall shear-stress distributions and velocity and turbulence fields) measurements were reported. It was for these same reasons that the Wigley hull was selected as the first test case of the basic viscous-flow method [14], including comparisons with some of the zero Fr data of the CEP. Herein, comparisons are made for zero Fr with this same data and for nonzero Fr with the appropriate data of the CEP. As will be shown later, the nonzero Fr data is not as complete or of the same quality as that for zero Fr, which was the motivation for a related experimental study for the Series 60 $C_B = 0.6$ ship model [28] for which calculations and comparisons are in progress. However, the comparisons are still useful in order to validate the present interactive approach and display the shortcomings of both the computations and experiments.

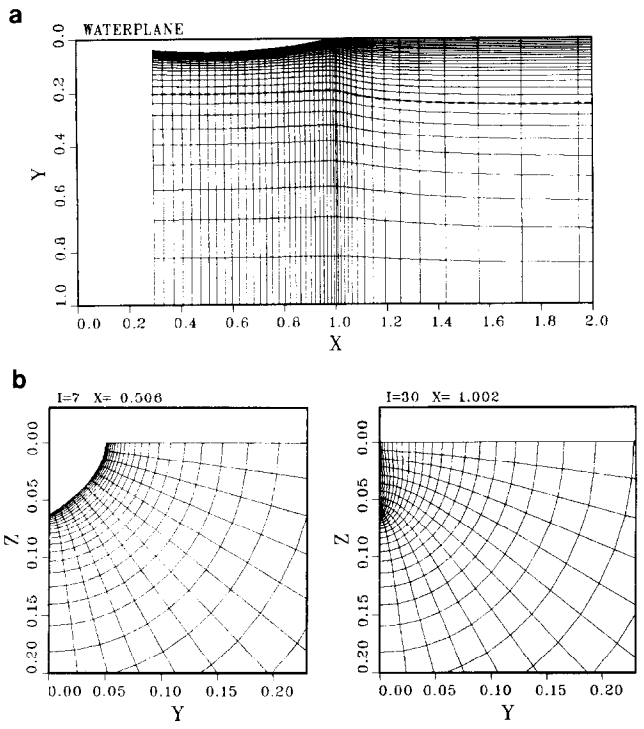

FIG. 2. Computational grid: (a) longitudinal plane; (b) body and wake crossplanes.

The coordinates of the Wigley hull are given by

$$y = \frac{B}{2}\{4x(1-x)\}\{1-(z/d)^2\}, \tag{35}$$

where $B = 0.1$ and $d = 0.0625$. Waterplane and typical crossplane views are shown in Fig. 2.

RESULTS

In the following, first, the computational grids (Figs. 2 and 3) and conditions are described. Then, some example results are presented and discussed for zero Fr, followed by those for nonzero Fr, including, wherever possible, comparisons with available experimental data, and, in the latter case, with inviscid-flow results. The convergence history of the pressure is shown in Fig. 4. Figure 5 provides a comparison of the large-domain and interactive solutions. The free-surface perspective view and contours, wave profile, and surface-pressure profiles and contours are shown in Fig. 6 through 10, respectively. The axial-velocity contours, crossplane-velocity vectors, and pressure, axial-vorticity, and turbulent kinetic energy contours for several representative stations are shown in Figs. 11 through 13. Lastly, the velocity, pressure, and turbulent kinetic energy profiles for similar stations are shown in Figs. 14 through 16. On the figures and in the discussions, the terminology "interactive" refers to results from both the interactive viscous and displacement-body inviscid solutions. When the distinction is not obvious it will be made. The terminology "inviscid" or "bare-body" refers to the noninteractive inviscid solution.

Computational Grids and Conditions

The viscous-flow computational grid was obtained using the technique of generating body-fitted coordinates through the solution of elliptic partial differential equations. Because of the simplicity of the present geometry, it is possible to specify the axial f^1 and circumferential f^3 control functions as, respectively, only functions of ξ and ζ; however, in order to accurately satisfy the body-surface boundary condition and resolve the viscous flow, $f^2 = f^2(\xi, \eta, \zeta)$. Partial views of the grids used in the calculations are shown in Figs. 2a, b for a longitudinal plane and typical body and wake crossplanes, respectively. Initially, a large-domain grid was generated. Subsequently, a small-domain grid was obtained by simply deleting that portion of the large-domain grid that lay beyond about $r > 0.2$. The outer boundary for the small-domain grid is shown by the dashed line in Fig. 2. For the large-domain grid, the inlet, exit, and outer boundaries are located at $x = (0.296, 4.524)$ and $r = 1$, respectively. The first grid point off the body surface is located in the range $90 < y^+ < 250$. Fifty axial, 30 radial, and 15 circumferential grid points were used. As already indicated, the small-domain grid was similar, except 21 radial grid points were used. In summary, the total number of grid points for the large- and small-domain calculations are 22,500 and 15,150, respectively.

The inviscid-flow displacement-body and free-surface panelization is shown in Fig. 3. Four hundred twenty three panels are distributed over the displacement body and 546 over the free surface for a total number of 969 panels. The panelization covers an area corresponding to 1-ship length upstream of the bow, 1.5-ship lengths in the transverse direction, and 3-ship lengths downstream of the stern. This panel arrangement was judged optimum based on panelization dependency tests [16].

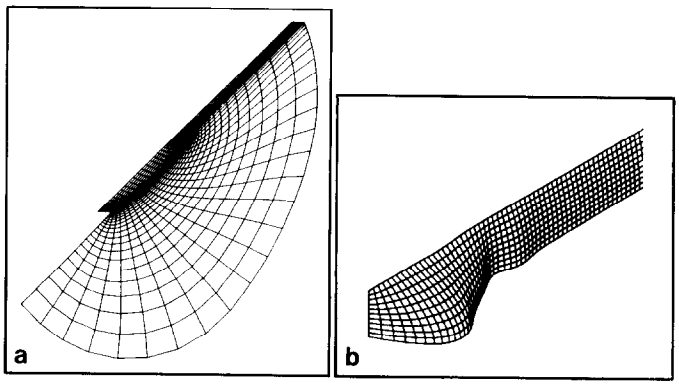

FIG. 3. Displacement bodies: (a) Fr = 0; (b) Fr = 0.316.

The conditions for the calculations are as follows: $L=1$; $U_0=1$; $\mathrm{Re}=4.5\times10^6$; $\mathrm{Fr}=0$ and 0.316; and on the inlet plane the average values for δ and U_τ are 0.0033 and 0.0455, respectively. These conditions were selected to correspond as closely as possible to those of the experiments of the CEP

Initially, large-domain calculations were performed for zero Fr. A zero-pressure initial condition was used and the values for the time α_t, pressure α_p, and transport quantity α_ϕ (where $\phi=k$ and ε) underrelaxation factors and total number of global iterations were 0.05 and 200, respectively. Next, small-domain calculations were performed, first for zero Fr, and then for nonzero Fr. For zero Fr, the interaction calculations were started with a zero-pressure initial condition and free-stream edge conditions ($U_e=1$, $W_e=p_e=0$). After 200 global iterations, the edge conditions were updated using the latest values of displacement thickness. Subsequently, the edge conditions were updated every 200 global iterations until convergence was achieved, which took three updates. For nonzero Fr, the calculations were started with the zero Fr solution as the initial condition and with nonzero Fr edge conditions obtained utilizing the zero Fr displacement body. This solution converged in 200 global iterations. Most of the results to be presented are for this case; however, some limited results will be shown in which the nonzero Fr edge conditions were obtained using an updated nonzero Fr displacement body. The values for α_t, α_p, and α_ϕ (where $\phi=k$ and ε) used for the small-domain calculations were the same as those for the large-domain calculations; however, for nonzero Fr, in addition, a value of 0.01 was used for α_ϕ (where $\phi=U$) for grid nodes near the outer boundary. The $\partial\hat{p}/\partial z$ term in (19) was found to have a small influence and was neglected in many of the calculations; however, this may be due, in part, to the present grid resolution. The calculations were performed on the Naval Research Laboratory CRAY XMP-24 supercomputer. The CPU time required for the calculations was about 17 min for 200 global iterations for the viscous-flow code and 1 min for the inviscid-flow code.

Extensive grid dependency and convergence checks were not carried out since these had been done previously both applications. However, some calculations were performed using both coarser and finer grids. These converged, respectively, more rapidly and slower than the present solution. Qualitatively the solutions were very similar to the present one, but with reduced and somewhat increased resolution, respectively. The convergence criterion was that the change in solution be less than about 0.05% for all variables. Usually the solutions were carried out at least 50 global iterations beyond meeting this criterion. Figure 4 provides the convergence history for the pressure and is typical of the results for all the variables. In Fig. 4, the abscissa is the global iteration number it and the ordinate is the residual $R(it)$, which is defined as

$$R(it)=\sum_{i=1}^{\mathrm{imax}}|p(i,it-1)-p(i,it)|\Big/\sum_{i=1}^{\mathrm{imax}}|p(i,\mathrm{itl})|, \quad (36)$$

where i, itl, and imax are the grid-point index and total number of iterations, and grid points, respectively. Referring to Fig. 4, global iterations 1–200 correspond to the final iterations of the zero Fr solution and global iterations 200–400 to those for the nonzero Fr solution.

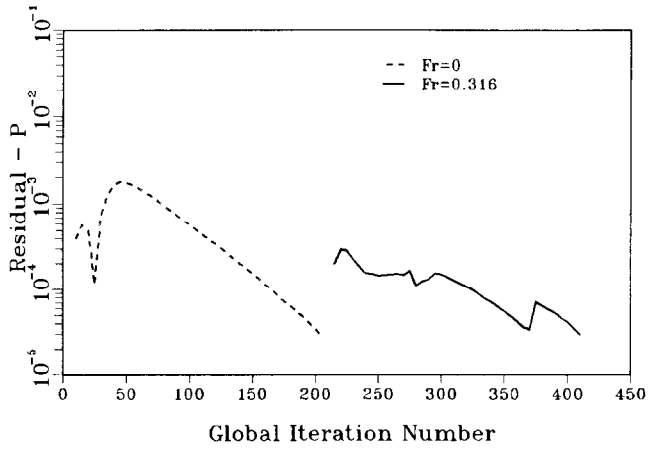

FIG. 4. Convergence history.

Zero Fr

Figure 5 provides a comparison of the zero Fr large-domain and interactive solutions and experimental data. The two solutions are nearly identical and show good agreement with the data, which validates the present interactive approach. The agreement with the data for the large-domain case is, of course, not surprising since this was already established in [14] for a similar grid and conditions, i.e., the present zero Fr solution is essentially the same as that of [14]. Some additional aspects of the zero Fr solution are displayed in Figs. 11 through 16 for later comparison with the nonzero Fr solution. Reference [14] provides detailed discussion of the zero Fr solution, including comparisons with the available experimental data. In summary, there is a downward flow on the forebody and an upward flow on the afterbody in response to the external-flow pressure gradients. The boundary layer and wake remain thin and attached and the viscous–inviscid interaction is weak; however, on the forebody, the boundary layer is relatively thicker near the keel than the waterplane, whereas the reverse holds true on the afterbody and in the near wake. The stern vortex is very weak. In the intermediate and far wake, the flow becomes axisymmetric.

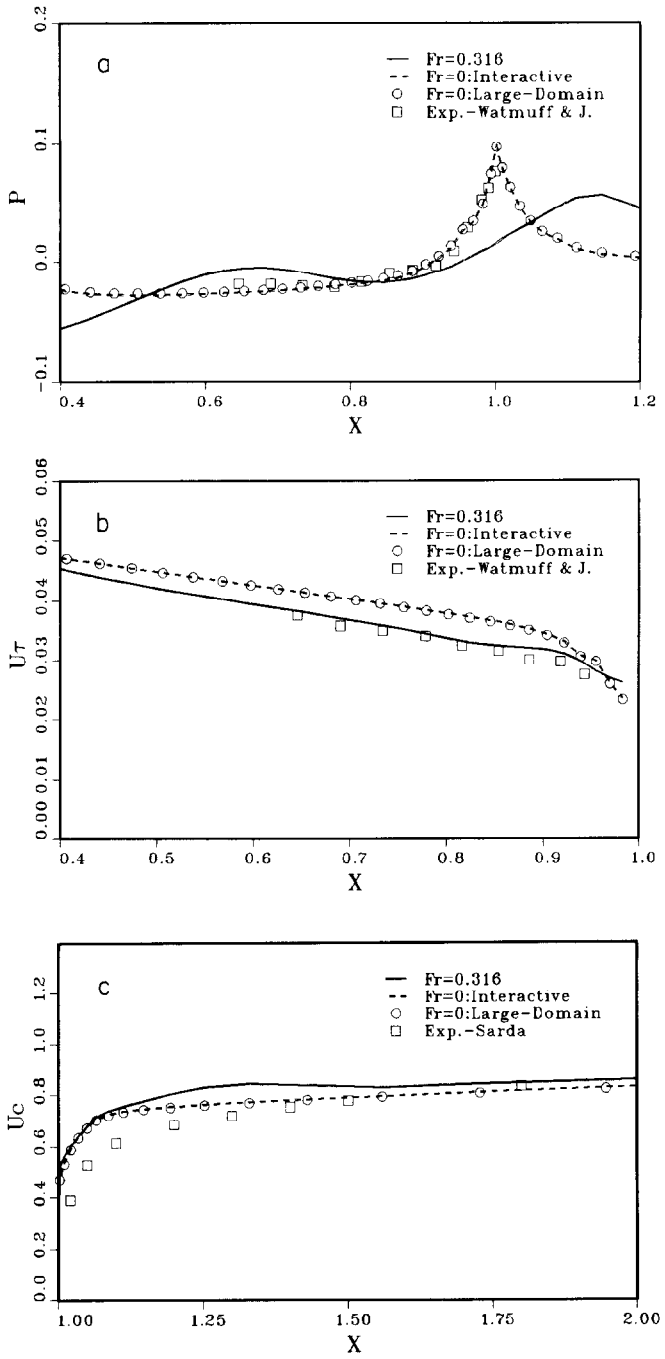

FIG. 5. Comparison of interactive and large-domain solutions, waterplane: (a) surface and wake centerplane pressure; (b) wall-shear velocity; (c) wake centerplane velocity.

As indicated in Figs. 5 and 14 through 16, the agreement between the calculations and data is quite good; however, there are some important differences, which are primarily attributed to the deficiencies of the standard $k-\varepsilon$ turbulence model with wall functions. In particular, the axial velocity and turbulent kinetic energy are overpredicted near the stern and there is a more rapid recovery in the wake.

Nonzero Fr

Figure 5 also includes nonzero Fr results for comparison. On the waterplane, the surface and wake centerplane pressure displays very dramatic differences, the wall-shear velocity shows similar trends, but with reduced magnitude, and the wake centerplane velocity indicates a faster recovery in the intermediate and far wake. As will be shown later, the first closely follows the wave profile, the second is due to an increase in boundary-layer thickness near the waterplane for the nonzero Fr case, and the third can be explained by the wave-induced pressure gradients. On the keel, all three of these quantities are nearly the same as for zero Fr.

The free-surface perspective views (Fig. 6) and contours (Fig. 7) vividly display the complex wave pattern consisting of both diverging and transverse wave systems. The bow and stern wave systems are seen to initiate with crests and the shoulder systems initiate with troughs, which conforms to the usual pattern described for this type of hull form. Very apparent is the reduced amplitude of the stern waves for the interactive as compared to the inviscid solution. Also, the diverging wave system is more pronounced and at a smaller angle with respect to the centerplane. Note that the axial and transverse wave-induced pressure gradients can be discerned from these figures, but with an appropriate phase shift, i.e., increasing and decreasing wave elevations imply, respectively, adverse and favorable gradients. The wave profile along the hull is shown in Fig. 8, which, in this case, includes experimental data for comparison. On the forebody, the two solutions are nearly identical and underpredict the amplitude of the bow-wave crest and the first trough. On the afterbody, the interactive solution indicates larger values than the inviscid solution, with the data in between the two. The wave profile for the nonzero Fr displacement body (Fig. 3b) is also shown in Fig. 8. The differences are minimal on the forebody, whereas, they are significant on the afterbody and depart from the data. It appears that the present simple definition (1) is insufficient for "wavy" displacement bodies.

The surface-pressure profiles (Fig. 9) show similar tendencies as just discussed with regard to the wave profile. On the forebody, the two solutions are nearly identical, but, in this case, in very close agreement with the data. The pressure on the forebody shown by the dashed line is that obtained from the inviscid displacement-body solution. On the afterbody, here again, the interactive solution indicates larger values than the inviscid solution, with the data in between the two. The wave-induced effects are seen to diminish with increasing depth and the agreement between the two solutions and the data on the afterbody shows improvement. The surface-pressure contours (Fig. 10) graphically display the differences between the two solutions and the data. Note that the axial and vertical surface-pressure gradients can be discerned from these figures, i.e.,

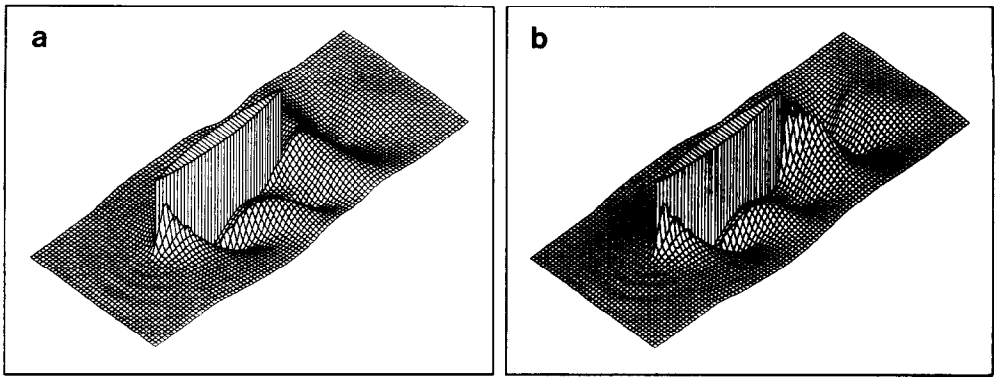

FIG. 6. Free-surface perspective view: (a) interactive; (b) inviscid.

increasing and decreasing pressure imply, respectively, adverse and favorable gradients. The larger wave elevation and pressure on the afterbody for the interactive solution results in the closed contours near the stern displayed in Fig. 10b. As already mentioned, the viscous–inviscid interaction is weak for the Wigley hull, which is the reason that the inviscid and viscous pressure distributions are quite similar. However, it appears that the interaction is greater for nonzero as compared to zero Fr.

Figures 11 through 13 show the detailed results for several representative stations, i.e., $x = 0.506$, 0.904, and 1.112, although the discussion to follow is based on the complete results at all stations. Note that for zero Fr the zero Fr, it is the predicted free surface. Also, the axial-velocity, -vorticity, and turbulent kinetic energy contours are not shown for the inviscid solution since, in the former case, their values are all very close to one and, in the latter two cases, they are, of course, zero. Solid curves indicate clockwise vorticity.

On the forebody (Fig. 11), the boundary layer is thin such that many aspects of the solutions are similar; however, there are some important differences. The nonzero Fr pressure fields show local and global effects of the free surface; i.e., near the free surface, regions of high and low pressure coincide with wave crests and troughs, respectively, and at larger depths, the contours are parallel to the

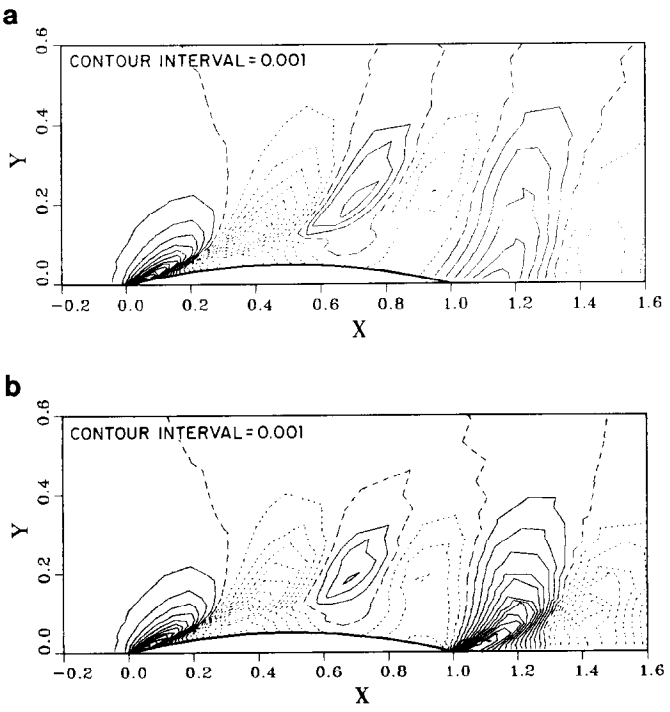

FIG. 7. Free-surface contours: (a) interactive; (b) inviscid.

vectors are considerably larger, especially for the interactive solution. The inviscid solution clearly lacks detail near the hull surface. The extent of the axial vorticity is increased for nonzero Fr and is locally influenced by the free surface. In both cases, as expected, the direction of rotation is mostly anticlockwise.

On the afterbody (Fig. 12), almost all aspects of the solutions show significant differences. The boundary layer

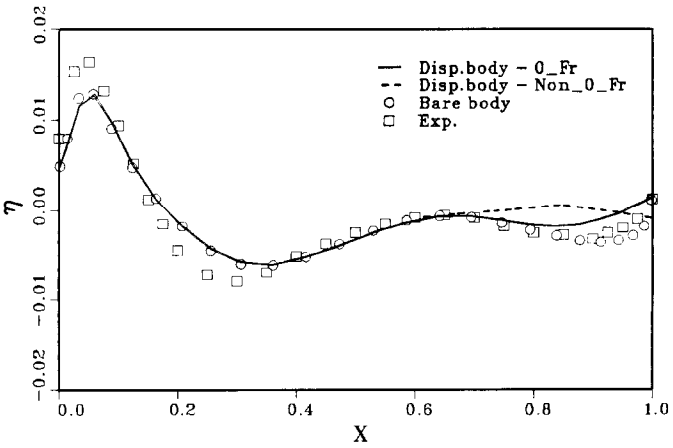

FIG. 8. Wave profile.

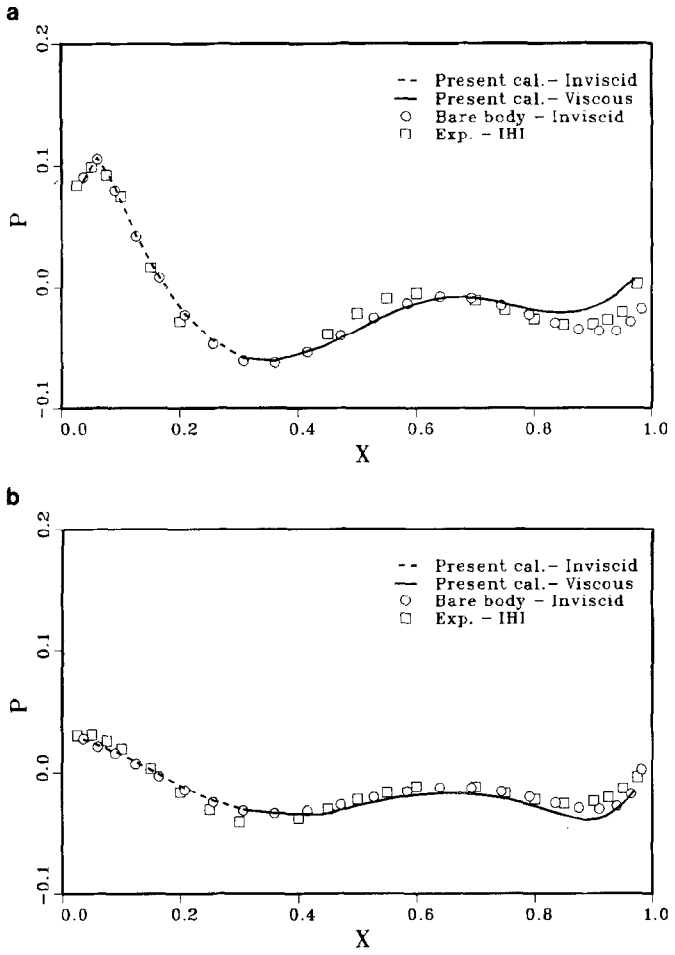

FIG. 9. Surface-pressure profiles: (a) $z/d = 0.04$; (b) $z/d = 0.92$.

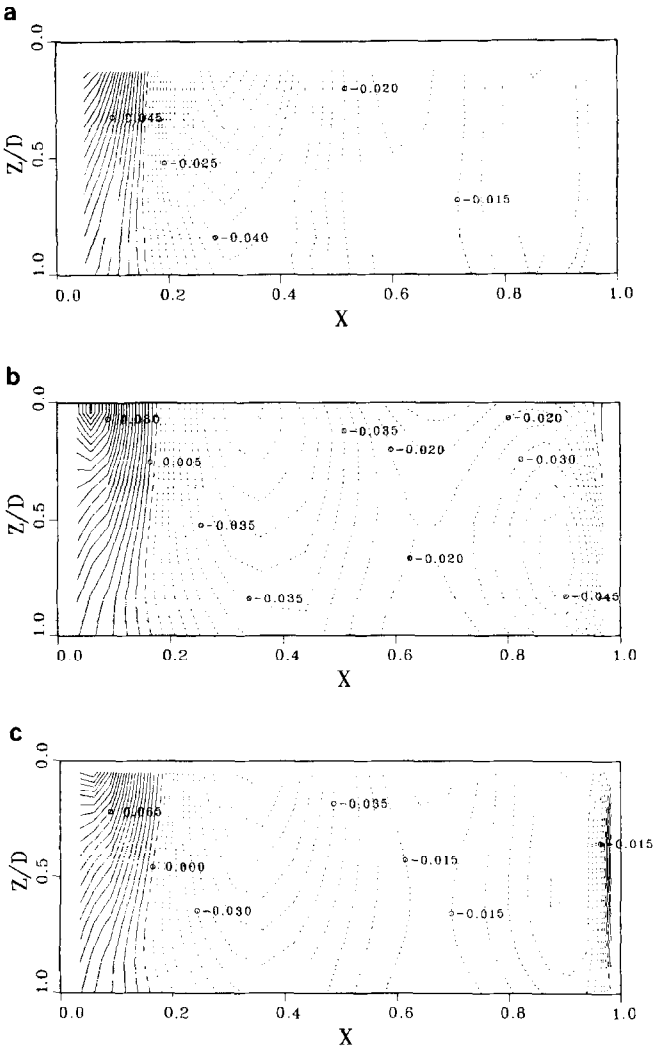

FIG. 10. Surface-pressure contours: (a) experiment; (b) interactive; (c) inviscid.

is thicker near the waterplane for nonzero as compared to zero Fr. This behavior begins at $x \approx 0.825$, which coincides with a region of adverse axial wave-induced pressure gradient (see Fig. 7). The differences for the pressure field and axial-vorticity contours are similar as described for the forebody; however, in the case of the crossplane-velocity vectors, there is an additional difference that, near the free surface, the interactive solution displays downward flow. This is consistent with the fact that the free-surface elevation is above the waterplane and the pressure is generally higher near the free surface than it is in larger depths, i.e., $\eta > 0$ and $\partial \hat{p}/\partial z < 0$. Note that, as expected, in both cases, the direction of rotation for the axial-vorticity is mostly clockwise. The turbulent kinetic energy contours are nearly the same for both Fr.

In the wake (Fig. 13), the solutions continue to show significant differences. Initially, the low-velocity region diffuses somewhat and covers a larger depthwise region; then, for $x > 1.2$, it recovers quite rapidly. A similar behavior was noted earlier for the wake centerline velocity for $x > 1.2$, both of which, as already mentioned, are consistent with the wave pattern. The zero Fr pressure field is nearly axisymmetric and fully recovered by the exit plane. The nonzero Fr pressure field continues to show free-surface effects, i.e., the contours are parallel to the free surface, but also fully recovered by the exit plane. Note the considerably larger wave elevation near the wake centerplane for the inviscid as compared to the interactive solution, which was pointed out earlier with regard to Figs. 6 and 7. Here again, the crossplane-velocity vectors are larger for nonzero as compared to zero Fr, especially near the wake centerplane for the interactive solution. The interactive and inviscid solutions display differences near the free surface, which appear to be consistent with the differences in their predicted wave patterns. The zero Fr axial vorticity decays fairly rapidly, whereas, for nonzero Fr, the decay is slow with a layer of nonzero vorticity persisting near the free surface all the way to the exit plane. The turbulent kinetic energy contours are similar for both Fr, but recover faster for the nonzero case.

Figures 14 through 16 show the velocity, pressure, and

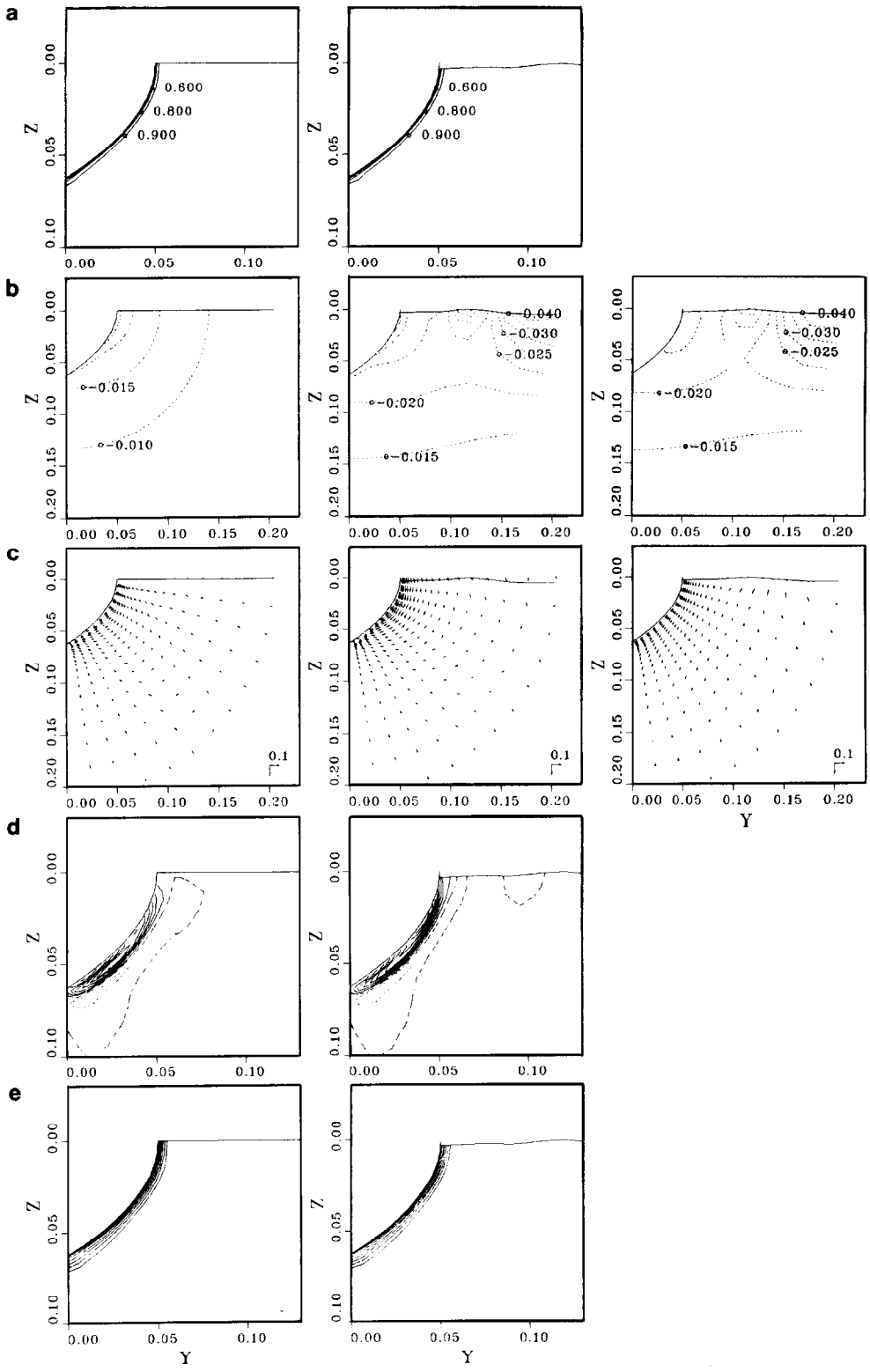

FIG. 11. Comparison of solutions at $x = 0.506$: (a) axial-velocity contours; (b) pressure contours; (c) crossplane-velocity vectors; (d) axial-vorticity contours; and (e) turbulent kinetic energy contours; columns, interactive, Fr = 0 and 0.316 and inviscid, Fr = 0.316, respectively.

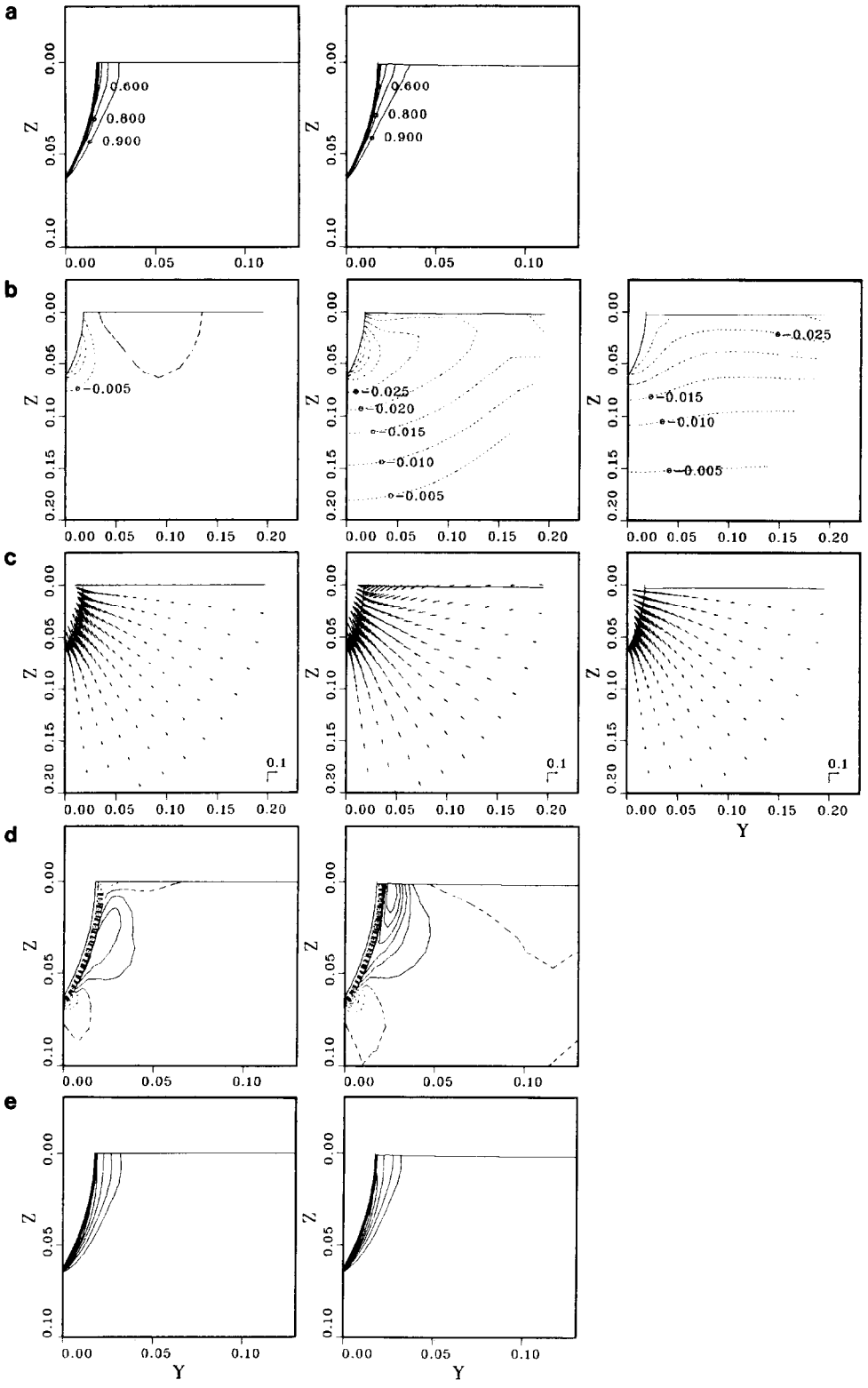

FIG. 12. Comparison of solutions at $x = 0.904$: (a) axial-velocity contours; (b) pressure contours; (c) crossplane-velocity vectors; (d) axial-vorticity contours; and (e) turbulent kinetic energy contours; columns, interactive, Fr = 0 and 0.316 and inviscid, Fr = 0.316, respectively.

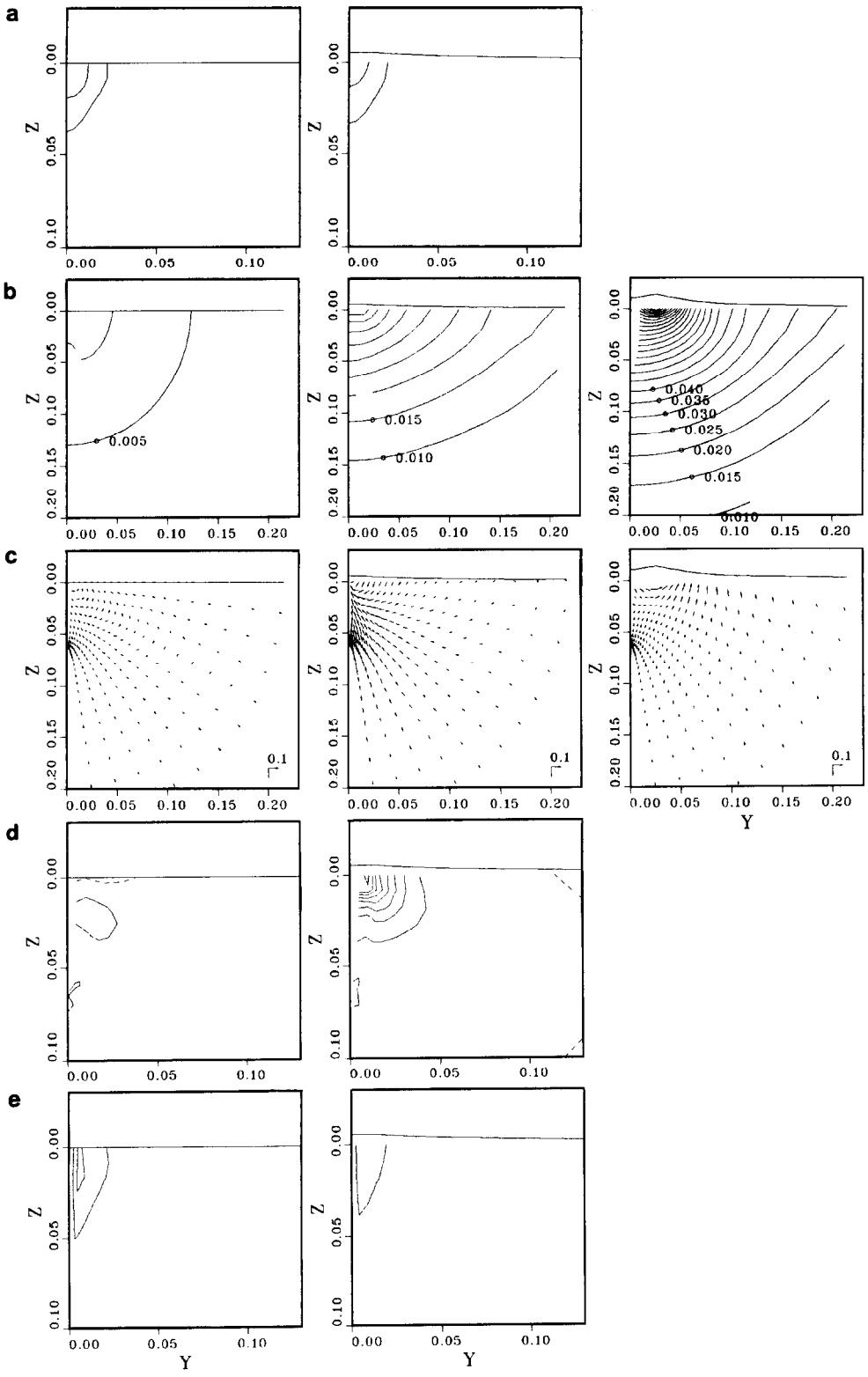

FIG. 13. Comparison of solutions at $x = 1.112$: (a) axial-velocity contours; (b) pressure contours; (c) crossplane-velocity vectors; (d) axial-vorticity contours; and (e) turbulent kinetic energy contours; columns, interactive, Fr = 0 and 0.316 and inviscid, Fr = 0.316.

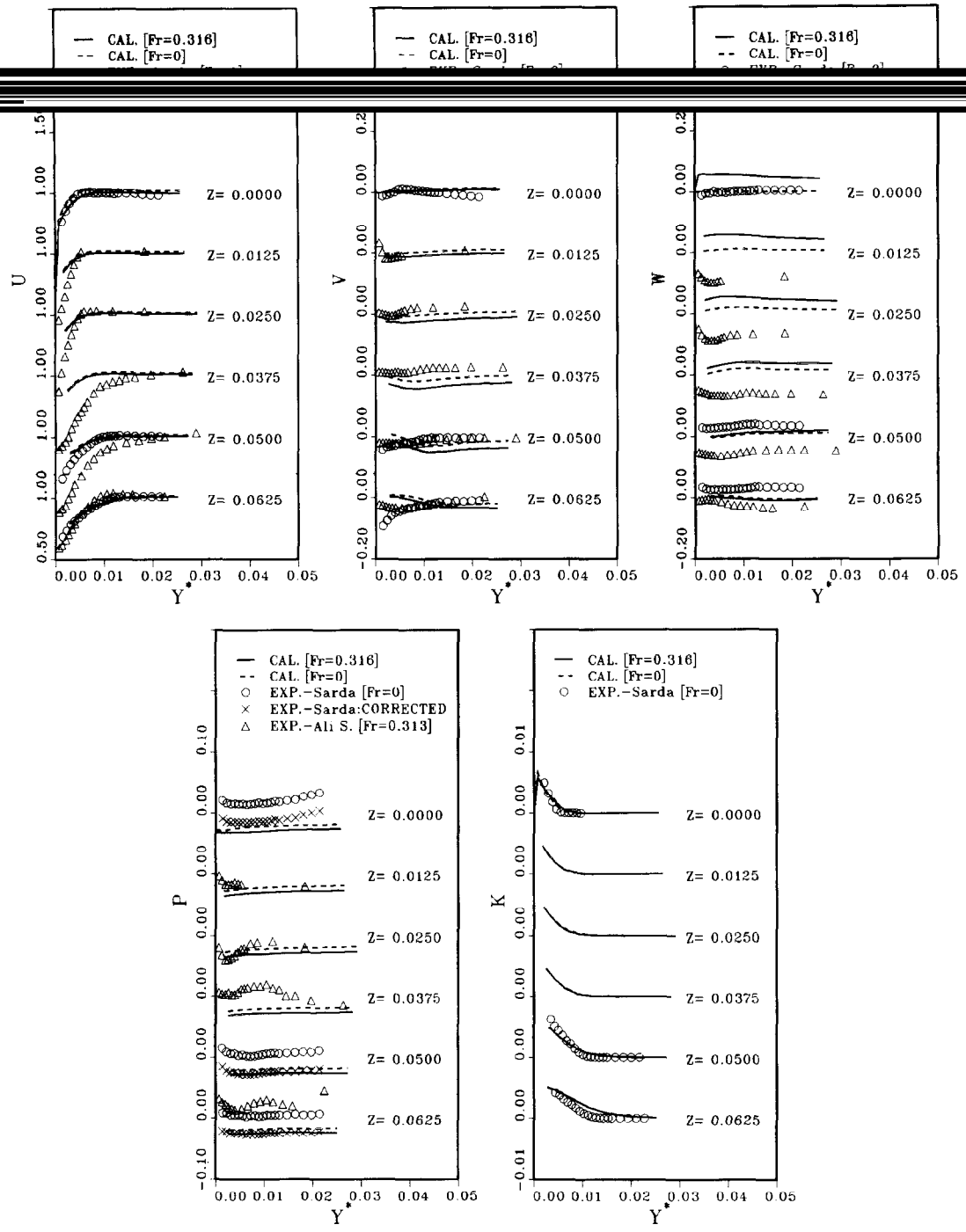

FIG. 14. Velocity, pressure, and turbulent kinetic energy profiles at $x = 0.5$.

turbulent kinetic energy profiles for similar stations as for Fig. 11 through 13, i.e., $x = 0.5$, 0.9, and 1.1. Also, included are both zero and nonzero Fr experimental data. At the largest two depths, $z = 0.05$ and 0.0625, data for both Fr are available, whereas, at the waterplane, $z = 0$, only zero Fr data are available. At the intermediate depths, data are available for both Fr, but for different z values. Since the interest here is primarily nonzero Fr and the zero Fr data and comparisons were already displayed in [14], only nonzero Fr data are shown for $z = 0.0125$, 0.025, and 0.0375. For zero Fr, a corrected pressure is also shown which includes a constant ($= -0.03$) reference-pressure correction as described in [14]. Turbulent kinetic energy data are only available for zero Fr.

At $x = 0.5$, consistent with previous discussions, the differences between the two solutions are quite small

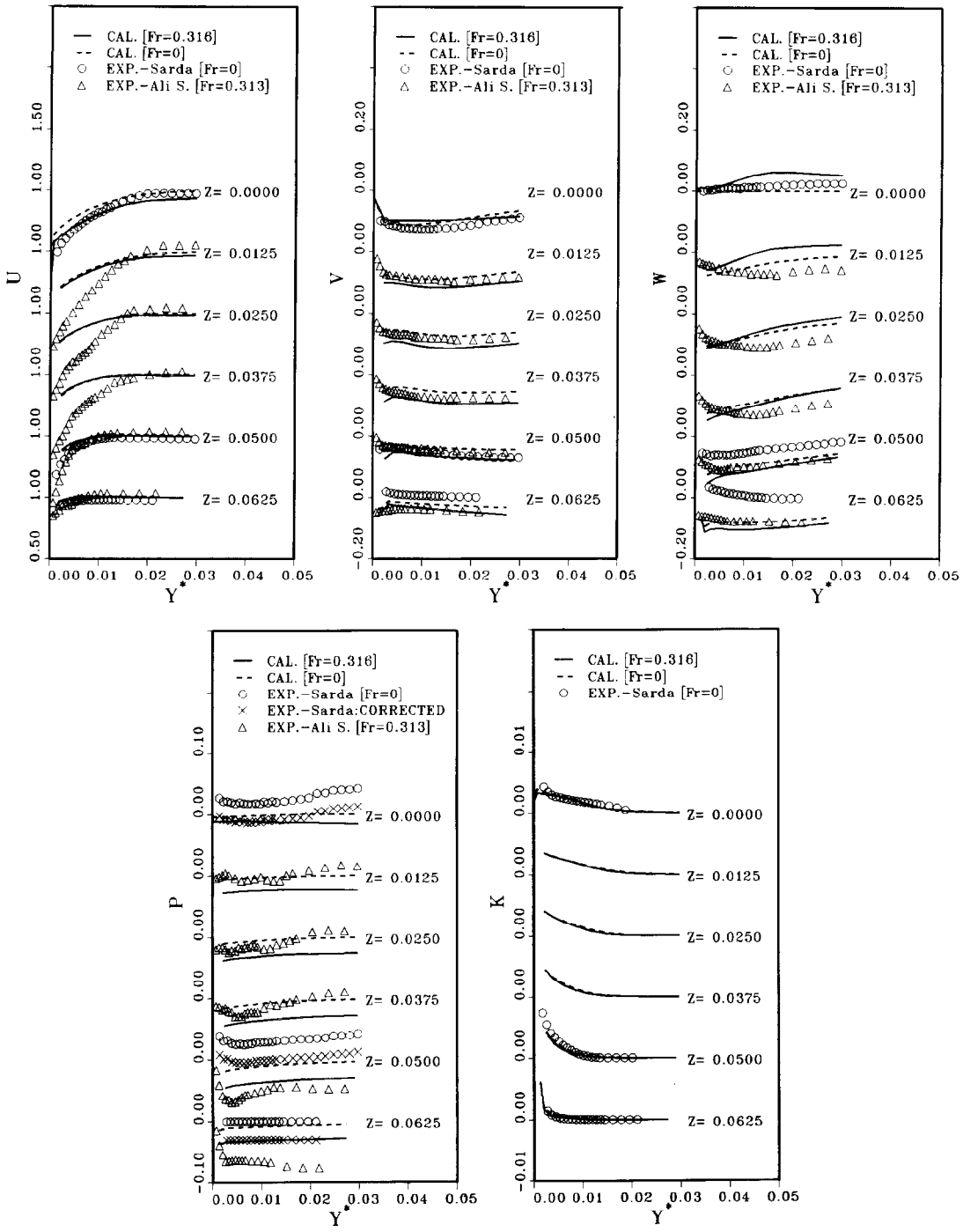

FIG. 15. Velocity, pressure, and turbulent kinetic energy profiles at $x = 0.9$.

and the agreemnt with the zero Fr data is good. However, the nonzero Fr data show some unexpected differences. In particular, the axial-velocity profile has a laminar appearance and the boundary-layer thickness is relatively large; the vertical velocity is upward, and the pressure shows considerable scatter. It is pointed out in [5] that the pressure-measurement error was appreciable.

At $x = 0.9$ and 1.1, here again, consistent with previous discussions, the differences between the two solutions are significant and the agreement between the zero Fr solution and data is good, except for the aforementioned discrepancies. The nonzero Fr solution shows larger axial velocities than the measurements for the inner part of the profiles. Here again, the measured profiles have a laminar appearance and the boundary layer is thick. However, no doubt a part of the difference is due to the calculations; i.e., as is the

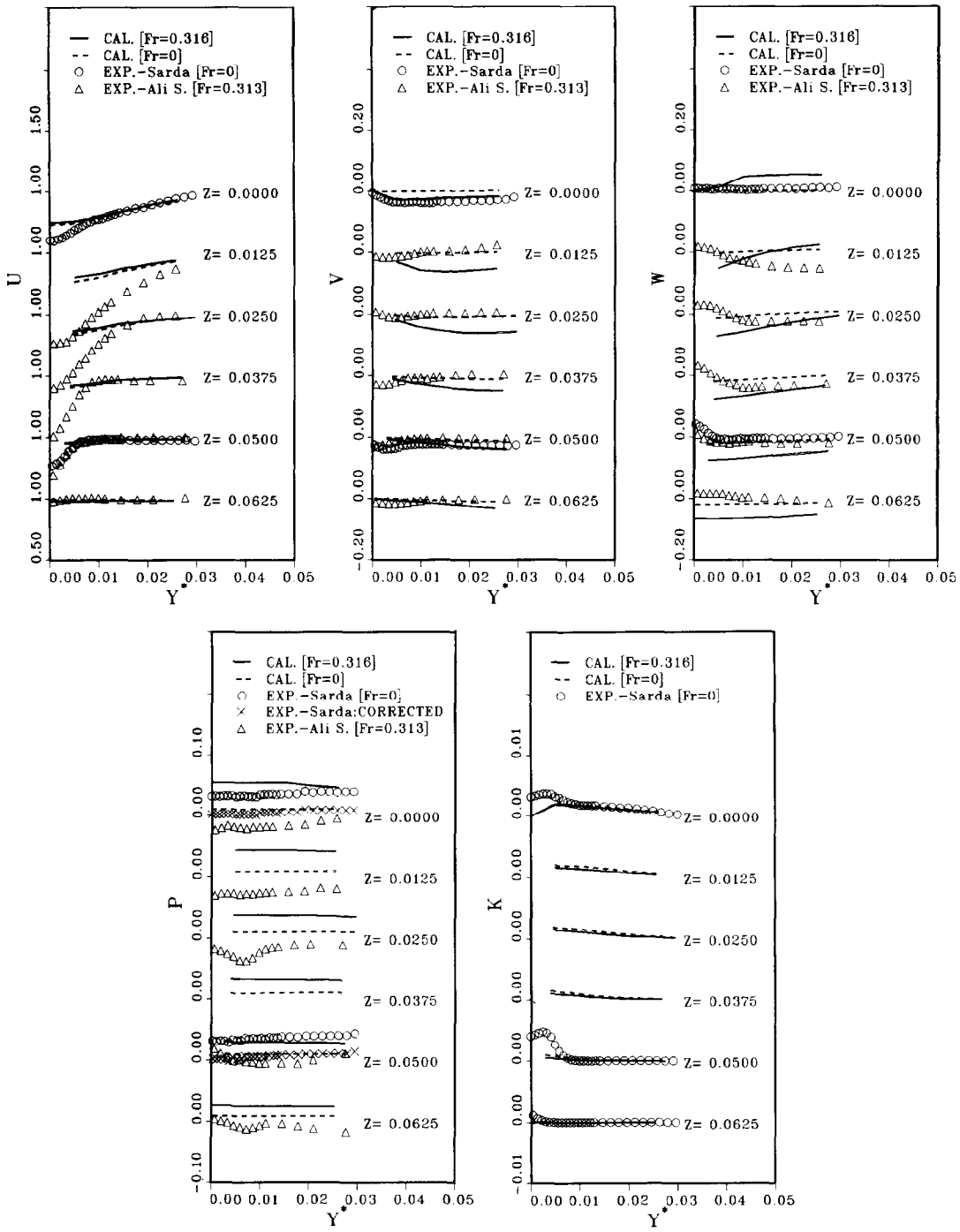

FIG. 16. Velocity, pressure, and turbulent kinetic energy profiles at $x = 1.1$.

case for zero Fr, due to deficiencies of the $k-\varepsilon$ turbulence model, an overprediction of the velocity near the wall and wake centerplane is expected. The transverse velocity is small and with similar trends for both calculations and measurements. The calculations indicate downward vertical velocities near the free surface and upward values for the midgirth region and near the keel. The agreement with the data near the keel is satisfactory, but in the midgirth region and near the free surface the data display greater upward flow than the calculations. In the wake, the nonzero Fr data show surprisingly small vertical velocities near the wake centerplane. Here again, the nonzero Fr pressure data shows considerable scatter and is difficult to compare with the calculations. Consistent with earlier discussions the turbulent kinetic energy profiles are nearly the same for both Fr.

TABLE I

Residuary-Resistance Coefficients

	L (m)	T (°C)	U_o (m/s)	Fr	Re	C_R
Experiment IHI	6	12.8	2.423	0.316	11.9×10^6	1.803×10^{-3}
Experiment SRI	4	10.6	1.978	0.316	6.14	1.998
Experiment UT	2.5	17.3	1.564	0.316	3.6	1.866
Inviscid	—	—	—	0.316	—	1.79
Interactive	—	—	—	0.316	4.5×10^6	1.92

Lastly, Table I provides a comparison of the calculated pressure-resistance coefficient and experimental values of the residuary-resistance (i.e., total frictional) coefficient. The experimental values cover a range of Re, including the present value, and clearly show a dependency on Re. Interestingly, the inviscid result compares well with the data at the highest Re, whereas the interactive result is close to that which the data implies at the present Re.

WAVE-BOUNDARY LAYER AND WAKE INTERACTION

The comparisons of the zero and nonzero Fr interactive and inviscid-flow results with experimental data enables an evaluation of the wave-boundary layer and wake interaction. Very significant differences are observed between the zero and nonzero Fr interactive results due to the presence of the free surface and gravity waves. In fact, the flow field is completely altered. Most of the differences were explicable in terms of the differences between the zero and nonzero Fr surface-pressure distributions and, in the latter case, the additional pressure gradients at the free surface associated with the wave pattern. The viscous–inviscid interaction appears to be greater for nonzero as compared to zero Fr. It should be mentioned that other factors undoubtedly have important influences, e.g., wave-induced separation, which are not included in the present theory.

The interactive and inviscid nonzero Fr solutions also indicate very significant differences. The inviscid solution clearly lacks "real-fluid effects." The viscous flow close to the hull and wake centerplane is clearly not accurately resolved. The interactive solution shows an increased response to pressure gradients as compared to the inviscid solution, especially in regions of low velocity. Also, the inviscid solution overpredicts the pressure recovery as the stern and the stern-wave amplitudes.

CONCLUDING REMARKS

The present work demonstrates for the first time the feasibility of an interactive approach for calculating ship boundary layers and wakes for nonzero Fr. The results presented for the Wigley hull are very encouraging. In fact, in many respects, the present results appear to be superior to the only other solutions of this type available, i.e., [10, 11]. This is true both with regard to the resolution of the boundary-layer and wake regions and the wave field. Furthermore, it appears that the present interactive approach is considerably more computationally efficient than the large-domain approaches of [10, 11]. This is consistent with the previous finding for zero Fr [15]. However, a complete evaluation of the present method was not possible. In the former case, due to the limited available experimental data. As mentioned earlier, a related experimental study for the Series 60 $C_B = 0.6$ ship model [28] was recently completed for which extensive measurements were made at both low and high Fr for which calculations and comparisons are in progress. In the latter case, due to the considerable differences in numerical techniques and algorithms and turbulence models between the present methods and those of [10, 11]. As mentioned earlier, the pursuit of a large-domain approach to the present problem is also of interest and will enable such an evaluation.

Finally, some of the issues that need to be addressed while further developing and validating the present approach are as follows: further assessment of the most appropriate free-surface boundary conditions; improved definition and construction of displacement bodies; the inclusion and resolution of the bow-flow region; extensions for lifting flow; and the ever present problem of grid generation and turbulence modeling. Also, of interest is the inclusion of nonlinear effects in the inviscid-flow code.

APPENDIX: NOMENCLATURE

A_ϕ, B_ϕ, etc.	Coefficients in transport equations
A_{ij}, B_{ij}, a_j, b_{jk}	Influence coefficients
b^i_j	Geometric tensor
C_D, C_P, C_U, C_{nb}	Finite-analytic coefficients (nb = NE, NW, SE, etc.)
C_f	Friction coefficient ($=2\tau_w/\rho U_o^2$)
C_p	Pressure coefficient
C_R	Residuary-resistance coefficient ($=2R/\rho S U_o^2$)
Fr	Froude number ($=U_o/\sqrt{gL}$)
g^{ij}	Conjugate metric tensor in general curvilinear coordinates ξ^i
k	Turbulent kinetic energy

L	Characteristic (ship) length
$\mathbf{n}$	Normal unit vector
$\hat{p}$	Piezometric pressure
R	Residuary resistance
Re	Reynolds number ($=U_o L/\nu$)
S	Wetted surface area
S_b, S_e, etc.	Boundaries of the solution domain
S_ϕ, S	Source functions
t	Time; arclength in tangential direction
$\mathbf{t}$	Tangent unit vector
U, V, W	Velocity components in cylindrical polar coordinates
U_x, V_y, W_z	Velocity components in Cartesian coordinates
U_c	Wake centerline velocity
U_o	Characteristic (freestream) velocity
U_τ	Wall-shear velocity ($=\sqrt{\tau_w/\rho}$)
$\overline{uu}$, $\overline{vv}$, etc.	Reynolds stresses
x, y, z	Cartesian coordinates
x, r, θ	Cylindrical polar coordinates
x^+, y^+, z^+	Dimensionless distances ($=U_\tau x/\nu$, etc.)
δ^*	Displacement thickness
ε	Rate of turbulent energy dissipation
η	Free-surface elevation
μ	Dipole strength
ν	Kinematic viscosity
ν_t	Eddy viscosity
ξ, η, ζ	Body-fitted coordinates
ρ	Density
σ	Source strength
τ	Time increment
τ_{ij}, τ_{ij}^*	Fluid- and external-stress tensors
τ_w	Wall-shear stress
ϕ	Transport quantities (U, V, W, k, ε); velocity potential

Subscripts

e	edge value
o	freestream or zero Fr value
p	inviscid-flow value

ACKNOWLEDGMENTS

This research was sponsored by the Office of Naval Research under Contract N00014-88-K-0113 under the administration of Dr. E. P. Rood whose support and helpful technical discussions are greatly appreciated.

REFERENCES

1. W. Lindenmuth, T. J. Ratcliffe, and A. M. Reed, DTRC/SHD-1260-1, 1988 (unpublished).
2. B. Rosen, South Bay Simulations Inc., Babylon, NY, private communication (1989).
3. V. C. Patel, in *Proceedings, 17th Office of Naval Research Symposium on Naval Hydrodynamics, The Hague, The Netherlands, 1988*, p. 217.
4. *Proc. 5th International Conference on Numerical Ship Hydrodynamics, Hiroshima, Japan, 1989.*
5. A. Shahshahan, Ph.D. thesis, The University of Iowa, Iowa City, IA, 1985 (unpublished).
6. M. Ikehata and Y. Tahara, *J. Soc. Naval Architects Jpn.* **161**, 49 (1987) [Japanese].
7. F. Stern, *J. Ship Res.* **30**, No. 4, 256 (1986).
8. F. Stern, W. S. Hwang, and S. Y. Jaw, *J. Ship Res.* **33**, No. 1, 63 (1989).
9. F. Stern, in *Proceedings, 4th International Conference on Numerical Ship Hydrodynamics, Washington, DC, 1985*, p. 383.
10. H. Miyata, T. Sato, and N. Baba, *J. Comput. Phys.* **72**, No. 2, 393 (1987).
11. T. Hino, in *Proceedings, 5th International Conference on Numerical Ship Hydrodynamics*, Hiroshima, Japan, 1989, p. 103.
12. F. H. Harlow and J. E. Welch, *Phys. Fluids* **8**, 2182 (1965).
13. R. K. C. Chan and R. L. Street, *J. Comput. Phys.* **6**, 68 (1970).
14. V. C. Patel, H. C. Chen, and S. Ju, Iowa Institute of Hydraulic Research, The University of Iowa, IIHR Report No. 323, 1988 (unpublished); *J. Comput. Phys.* **88**, No. 2, 305 (1990).
15. F. Stern, S. Y. Yoo, and V. C. Patel, *AIAA J.* **26**, No. 9, 1052 (1988).
16. J. Longo, M.S. thesis, The University of Iowa, Iowa City, IA, 1990 (unpublished).
17. R. Black, M.S. thesis, The University of Iowa, Iowa City, IA, 1991 (unpublished).
18. T. Hotta and S. Hatano, in *Fall Meeting of the Society of Naval Architects of Japan, 1983.*
19. W. Rodi, "Turbulence Model and Their Application in Hydraulics," presented at the IAHR Section on Fundamentals of Division II: Experimental and Mathematical Fluid Dynamics, 1980 (unpublished).
20. T. F. Swean and R. D. Peltzer, NRL Memo Report 5426, Naval Research Laboratory, Washington, DC, 1984 (unpublished).
21. S. E. Ramberg, T. F. Swean, and M. W. Plesniak, NRL Memo Report 6367, Naval Research Laboratory, Washington, DC, 1989 (unpublished).
22. B. Maskew, *J. Aircraft* **19**, No. 2, 157 (1982).
23. B. Maskew, NASA CR-166476, 1982 (unpublished).
24. C. W. Boppe, B. S. Rosen, J. P. Laiosa, and B. Chance, Jr., "*Stars & Stripes '87*: Computational Flow Simulations for Hydrodynamic Design," the Eighth Chesapeake Sailing Yacht Symposium, Annapolis, MD, 1987 (unpublished).
25. F. Stern, *ASME J. Fluids Eng.* **111**, 290 (1989).
26. C. W. Dawson, in *Proceedings, 2nd International Conference on Numerical Ship Hydrodynamics, Berkeley, CA 1977*, p. 30.
27. "Report of the Resistance and Flow Committee," in *Proceedings, 18th Int. Towing Tank Conf., Kobe, Japan, 1987*, p. 47.
28. Y. Toda, F. Stern, and J. Longo, Iowa Institute of Hydraulic Research, The University of Iowa, IIHR report, 1991 (unpublished).
29. O. P. Sarda, Ph.D. thesis, The University of Iowa, Iowa City, IA, 1986 (unpublished).
30. H. Kajatani, H. Miyata, M. Ikehata, H. Tanaka, H. Adachi, M. Namimatsu, and S. Ogiwara, in *Proceedings, 2nd DTNSRDC Workshop on Ship Wave-Resistance Computations, 1983*, p. 5.